JAAS

ROYAL SOCIETY OF CHEMISTRY

PAPER

View Article Online
View Journal

Cite this: DOI: 10.1039/d5ja00468c

Separation and characterization of gold nanomaterials with different shapes using AF4-ICP-MS and single-particle ICP-MS

Yu-ki Tanaka, * Sana Hasegawa and Yasumitsu Ogra

The toxicity profiles of nanomaterials (NMs) are affected by their chemical composition, size, and shape. Inductively coupled plasma mass spectrometry (ICP-MS) is a robust, element-specific analytical tool for detecting the chemical composition of NMs. Fast time-resolved analysis by single-particle ICP-MS (spICP-MS) enables the discrimination of individual nanoparticles and the determination of their sizes based on elemental content. However, because spICP-MS evaluates particle sizes on the basis of their elemental mass, it cannot distinguish differently shaped NMs with identical volume. In this study, we used asymmetric flow field-flow fractionation coupled with ICP-MS (AF4-ICP-MS) to separate gold NMs of different shapes. Although clear separation was not achieved with AF4-ICP-MS, the signal intensities of NMs with similar volumes but different shapes varied significantly in spICP-MS analysis; namely, nanorods and nanoplates exhibited lower signal intensities than nanospheres with similar volumes. These results suggest that the ionization efficiency of NMs in the ICP is influenced by particle shape, with incomplete ionization preferentially occurring in nanorods and nanoplates. Our findings demonstrate the potential of spICP-MS for shape-dependent separation and characterization of NMs.

Received 26th November 2025
Accepted 13th February 2026

DOI: 10.1039/d5ja00468c

rsc.li/jaas

Introduction

Nanomaterials (NMs) are used in various industrial fields, including electronics, agriculture, food processing, biotechnology, and pharmaceuticals. Owing to their unique physicochemical properties, which depend on their chemical composition, size, shape, and surface modification, NMs have diverse applications.[1] The toxicity of NMs has also been reported to vary depending on their physicochemical properties.[2–6] Therefore, the characterization and quantitative determination of NMs with different compositions, sizes, and shapes are essential to better understand their toxicity.

Recent advances in nanotechnology have led to the development of analytical methods for characterizing NMs. These methods include electron microscopy, dynamic or static light scattering, and inductively coupled plasma mass spectrometry (ICP-MS). ICP-MS enables element-specific detection of NMs, identifying their chemical composition. Unlike conventional elemental analysis, NM suspensions can be analyzed by ICP-MS without acid digestion.

There are two promising analytical approaches for characterizing NM suspensions using ICP-MS. One is the detection of individual NMs in the fast time-resolved mode (single-particle ICP-MS; hereinafter, spICP-MS).[7,8] In this method, time-resolved analysis is performed with a signal integration period shorter than 1 ms to capture transient signals generated by single NMs, which typically last for approximately 0.5 ms.[9] Because particles are detected individually, spICP-MS can efficiently analyze samples with low concentrations of suspended particles. Particle size can be calculated from the detected elemental mass, assuming a specific particle shape. Another approach is the size-based separation of NMs using field-flow fractionation (FFF) techniques, such as asymmetric flow (AF4)[10–12] and centrifugal flow (CF3),[13] in combination with ICP-MS. Here, we focus on AF4, which is commonly used in NM analysis. AF4 separates NMs in a liquid flow by applying a cross-flow. After cross-flow application, NMs diffuse in the direction opposite to the cross-flow, and their equilibrium positions are dependent on the diffusion coefficient (D). For spherical particles, D is inversely proportional to their diameter. Hence, smaller particles with larger D values migrate to regions with higher flow velocities in a parabolic velocity profile, and elute earlier from the AF4 channel.[10] Particle size can be determined by coupling multi-angle light scattering (MALS).[14,15] In addition, comparing the elution times of NMs with those of nanoparticle standards of known sizes[16] or performing theoretical calculations[17] provides reliable particle size information.

Although ICP-MS-based approaches yield information on elemental composition and particle size, capturing particle shape remains challenging. López-Sanz *et al.* reported the potential for shape-dependent separation of NMs by AF4-ICP-MS.[18] However, they used nanospheres and nanorods with different volumes, which can also be fundamentally

Graduate School of Pharmaceutical Sciences, Chiba University, 1-8-1 Inohana, Chuo, Chiba 260-8675, Japan. E-mail: yu-ki.tanaka@chiba-u.jp; Fax: +81 43 226 2945

distinguished by spICP-MS. Because NM separation by AF4-ICP-MS is based on differences in D values, this technique is applicable to the shape differentiation of NMs with similar volumes, which cannot be accomplished by spICP-MS. Therefore, in this study, we examined the possibility of distinguishing differently shaped gold nanomaterials (AuNMs) with similar volumes by AF4-ICP-MS.

Materials and methods

Reagents

Four different AuNMs—nanospheres with diameters of 100 nm and 120 nm (NS-100-50 and NS-120-50; NanoSeedz Ltd, Hong Kong, China), hexagonal nanoplates (GNPL-790-20; NanoSeedz Ltd), and nanorods (A12-50-1064-CTAB-DIH-1; Nanopartz, Inc., Loveland, CO, USA)—were used in this study. Details of the AuNMs are summarized in Table 1. NMs with identical volumes but different shapes were commercially unavailable. Therefore, two groups of NMs with similar volumes but different shapes were used for ICP-MS analysis. The volume of the 100 nm nanospheres (5.24×10^5 nm^3) was similar to that of the nanorods (5.20×10^5 nm^3), with a deviation of approximately 1.0%. The volume of the 120 nm nanospheres (9.05×10^5 nm^3) was close to that of the nanoplates (7.79×10^5 nm^3), with a deviation of approximately 16%.

An ionic Au standard solution was purchased from Kanto Chemical Co., Inc. (Tokyo, Japan). L-cysteine and methanol (FUJIFILM Wako Pure Chemical Corporation, Osaka, Japan) were used to dilute the ionic Au and AuNMs. Silica nanoparticles (200 nm i.d., Sigma-Aldrich, Saint Louis, MO, USA) and an ionic silicon standard solution (Kanto Chemical Co., Inc.) were used to determine the transport efficiency from the nebulizer to the ICP. Milli-Q water with a specific resistance of 18.2 MΩ cm^{-1} (Merck Millipore, Burlington, MA, USA) was used throughout the study.

Separation of AuNMs by AF4-ICP-MS

AuNM suspensions were prepared as follows. AuNMs were diluted with Milli-Q water to 1.0 μg mL^{-1} for group 1 NMs and 0.6 μg mL^{-1} for group 2 NMs. A 20 μL aliquot of each NM suspension was injected into an AF4 system (AF2000, Postnova Analytics, Landsberg, Germany) and eluted with 0.01% Nova-Chem Surfactant 100 solution (Postnova Analytics). The operational conditions of the AF4 system are summarized in Table 2. We optimized the AF4 parameters to improve the resolution for the two NMs in each group. The eluent from the AF4 channel was continuously introduced into an ICP-MS (Agilent 8800 ICP-MS/MS, Agilent Technologies, Tokyo, Japan). ^{197}Au signal intensity was monitored in the time-resolved analysis mode without using a collision/reaction cell (no-gas mode). The ICP-MS operational conditions are also summarized in Table 2.

Characterization of AuNMs by spICP-MS

Each AuNM suspension was diluted 100-fold with 1% methanol, and then diluted further with 0.01% L-cysteine solution to a concentration of 1.0×10^5 particles per mL. An ionic Au solution at 100 ng mL^{-1} was prepared by diluting with a 0.01% L-cysteine solution. To determine the elemental contents from individual pulsed signals of NMs, calibration was performed using a method previously established for single-cell elemental analysis.[19] Transport efficiency determined through the measurement of Milli-Q water, ionic silicon, and silica nanoparticle solutions was 53.6%. The sensitivity factor (cps/(ng mL^{-1})) obtained from the ionic Au solution was corrected using the transport efficiency. Finally, the signal intensity of AuNMs was calibrated using the corrected sensitivity factor to obtain the mass of Au in each NM. All calculations were carried out using MassHunter software (Agilent Technologies) with automatic particle baseline correction.

Both sample and standard solutions were introduced through a concentric glass nebulizer (MicroMist, Glass Expansion, Victoria, Australia) and a total consumption spray

Table 1 AuNMs used in this study

	Group 1		Group 2	
	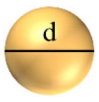	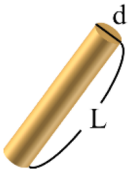	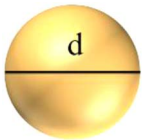	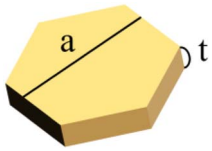
Shape	Sphere	Rod	Sphere	Plate
Nominal size (nm)	$d = 100$	$d = 50$ $L = 265$	$d = 120$	$a = 150$ $t = 40$
Surface area (nm^2)	3.14×10^4	4.56×10^4	4.52×10^4	5.98×10^4
Volume (nm^3)	5.24×10^5	5.20×10^5	9.05×10^5	7.79×10^5
Specific surface area (1/nm)	0.0600	0.0876	0.0500	0.0768
Coating[a]	CTAB	CTAB	CTAB	CTAB

[a] CTAB: cetyltrimethylammonium bromide.

Table 2 Instrumentation and operational settings

AF4 system	
Instrument	AF2000 (Postnova)
Spacer thickness	350 μm
Eluent	NovaChem (0.01%) in Milli-Q water
Sample volume	20 μL
Detection flow rate	1.0 mL min^{-1}
Injection flow rate	0.2 mL min^{-1}
Injection time	7.5 min (including 0.5 min transition time)
Focus flow rate	1.8 mL min^{-1}
Cross-flow rate	1.0 mL min^{-1}
Cross-flow gradient	Power function ($k = 0.5$), 1.0 mL min^{-1} to 0 mL min^{-1} for 20 min (group 1), for 30 min (group 2)
ICP-MS (for AF4)	
Instrument	Agilent 8800 (Agilent Technologies)
ICP incident power	1600 W
Cooling gas flow rate	15.0 L min^{-1}
Auxiliary gas flow rate	0.80 L min^{-1}
Nebulizer gas flow rate	1.0 L min^{-1}
Collision/reaction cell	No gas
Integration time	1.0 s
Monitored isotope	^{197}Au
Signal monitoring period	25 min
ICP-MS (for single particle)	
Instrument	Agilent 8900 (Agilent Technologies)
ICP incident power	1600 W
Cooling gas flow rate	15.0 L min^{-1}
Auxiliary gas flow rate	0.80 L min^{-1}
Nebulizer gas flow rate	0.6 L min^{-1}
Collision/reaction cell	No gas for Au, H_2 (5.5 mL min^{-1}) for Si
Integration time	0.1 ms
Monitored isotope	^{197}Au, ^{28}Si
Signal monitoring period	40 s for Au, 15 s for Si

chamber (Single-Cell Sample Introduction System for Agilent ICP-MS, Glass Expansion) at a flow rate of 15 μL min^{-1}. We monitored the signal intensities of ^{197}Au in the no-gas mode and ^{28}Si in the H_2 collision mode using ICP-MS (Agilent 8900 ICP-MS/MS, Agilent Technologies). The number of transient signals from AuNMs within a 40 s signal monitoring period was counted. The transport efficiency of AuNMs was calculated as the ratio of the number of transient signals to the number of particles introduced into the ICP-MS for 40 s. Measurements were repeated three times for each sample. The ICP-MS operational conditions are also summarized in Table 2.

Results and discussion

Separation of AuNMs by AF4-ICP-MS

The fractograms of the four AuNMs are shown in Fig. 1. Due to diffusion within the AF4 channel, the peaks were broad, extending over approximately 5 minutes. This is typical for separation using the AF4 channel.[4] In group 1, nanorods eluted first (18.8 min), followed by nanospheres (19.8 min). Although both NMs contained the same amount of Au, the signal intensity of nanorods was much lower than that of nanospheres. For group 2, nanospheres (19.2 min) eluted first, followed by nanoplates (20.2 min).

In AF4 separation, the elution time is determined by the D values of particles in the liquid phase.[17] For spherical particles, D is inversely proportional to their diameter. Thus, smaller particles elute earlier under identical conditions. However, for rod- and plate-shaped particles, understanding their D values quantitatively is complicated. To clarify the translational D values for rod-shaped particles, the following equation (eqn (1)), which was modified from the basic FFF equation for spherical particles,[20] was applied to AF4-ICP-MS data.[18,21,22]

$$D = \frac{V_c \omega^2}{12 V_0} \frac{t_0}{t_r} \quad (1)$$

V_c is the cross-flow rate, V_0 is the channel void volume, ω is the channel thickness, t_0 is the void time, and t_r is the observed elution

time. Based on the present parameters (V_c = 0.50 mL min^{-1} (average from 7.5 min to 18.8 min), V_0 = 1.147 mL, $\omega = 350 \times 10^{-6}$ m, t_0 = 0.67 min, and t_r = 11.8 min), D was calculated as 4.2 × 10^{-12} m^2 s^{-1}. In addition, D for rod-shaped NMs is defined in the mathematical model by the following equation (eqn (2)):

$$D = \frac{k_B T}{12\pi\eta L}\alpha \quad (2)$$

where k_B is the Boltzmann constant, T is the absolute temperature, η is the viscosity, L is the rod length, and α is an empirically obtained factor based on the aspect ratio (L/d) of rod-shaped NMs.[21,23] Here, we obtained a D value of 3.4 × 10^{-12} m^2 s^{-1} using the following parameters: T = 293 K, η = 0.001 kg m^{-1} s^{-1}, $L = 265 \times 10^{-9}$ m, and α = 2.08. Because these two D values showed good agreement, the previously reported model for the elution behavior of rod-shaped NMs would be useful for estimating the elution time in AF4 analysis. In our previous study, silica nanospheres with a 20 nm difference in diameter eluted approximately 2 min apart, which was sufficient to resolve each component in the fractogram of their mixture. In the present study, if the same volume of nanorods with an aspect ratio of 10.4 (*i.e.*, L = 414 nm, d = 40 nm) were used, the elution time would be approximately 3.0 min later than that of the current nanorods (L = 265 nm, d = 50 nm), resulting in clearer separation from nanospheres. This consideration also applies to the NMs in group 2, namely, if nanoplates with the same volume but different length-to-thickness ratios were used, their separation from nanospheres would become more pronounced.

In AF4, non-spherical particle behavior is classified into three modes depending on how far the particles are distributed from the accumulation wall, which is determined by the cross-flow rate and D.[24] These are the steric mode ($D/U < 0.5d$), the steric–entropic mode ($0.5d < D/U < 0.5L$), and the normal (Brownian) mode ($D/U > 0.5L$), where U is the cross-flow rate. In this study, the cross-flow rate before NM elution was at most 1.0 mL min^{-1}, corresponding to a linear velocity of approximately 5.1 × 10^{-6} m s^{-1}. On the other hand, D was 3.4 × 10^{-12} m^2 s^{-1}, providing D/U of approximately 6 × 10^{-7} m = 600 nm. Therefore, we considered that the AuNMs eluted in the normal mode depending on their D values. Park and Mittal reported that rod-shaped particles have smaller D values than spherical particles of the same volume in the normal mode, resulting in slower elution.[25] In contrast, in the present study, nanorods eluted slightly earlier than nanospheres with almost the same volume, which could not be explained by this theoretical estimation. Since particle behavior in AF4 depends on hydrodynamic size, the 100 nm nanospheres may have a hydrodynamic diameter larger than 100 nm and therefor eluted later than the nanorods.

Characterization of AuNMs by spICP-MS

We measured the four types of AuNMs using spICP-MS. Transient pulsed signals with a signal duration of approximately 0.5

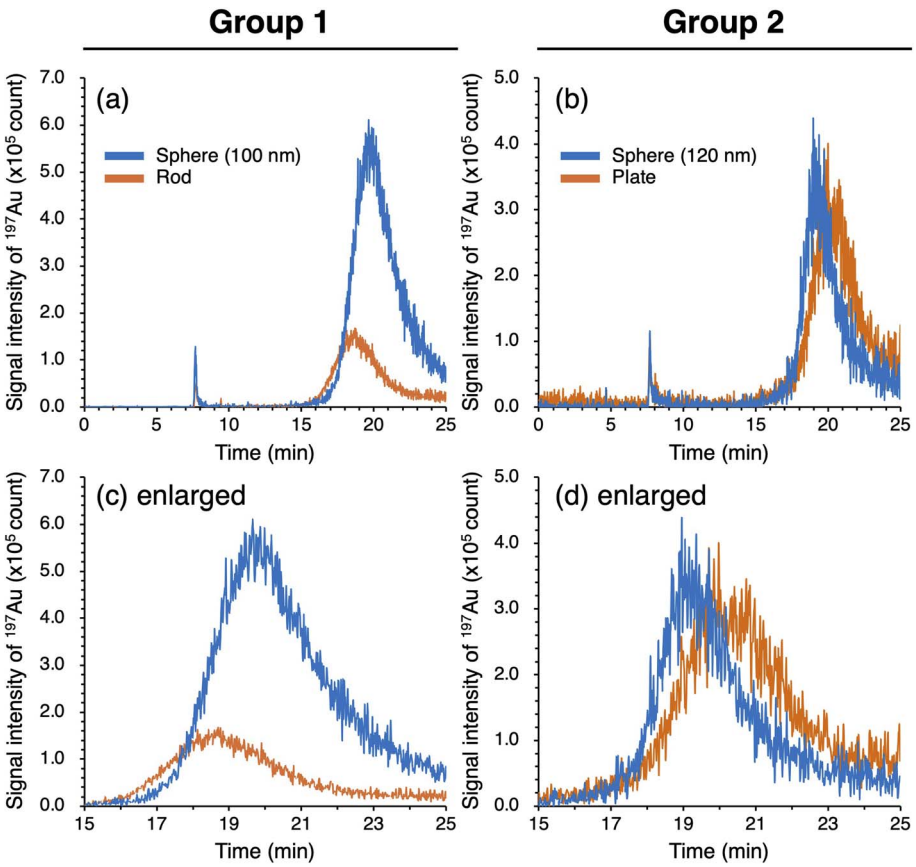

Fig. 1 Fractograms of AuNMs detected by AF4-ICP-MS. Panels (c) and (d) are enlarged fractograms of panels (a) and (b), respectively.

ms were detected in fast time-resolved analysis (Fig. 2). The average number of pulsed signals detected within the 40 s signal monitoring period was 336 for 100 nm nanospheres, 462 for nanorods, 435 for 120 nm nanospheres, and 545 for nanoplates ($n = 3$). As 1000 particles were theoretically introduced into the ICP-MS during this period, the transport efficiencies of the AuNMs were calculated as follows: 33.6 ± 2.1% for 100 nm nanospheres, 46.2 ± 4.7% for nanorods, 43.5 ± 8.3% for 120 nm nanospheres, and 54.5 ± 5.9% for nanoplates (mean ± SD, $n = 3$) (Table 3). Although these values were in good agreement with the transport efficiency evaluated using silica nanoparticles (53.6%), approximately 60% deviations were found between 100 nm nanosphere and silica nanoparticles. This discrepancy can be attributed to instability in the sample flow rate when using a microsyringe pump at very low flow rate, which lead to variations in the volume of sample introduced during the signal monitoring period. In addition, differences in the physicochemical properties of silica and gold may affect particle aggregation and adsorption onto plastic tubing after dilution with MQ water, thereby changing the number density of the NMs.

The intensity of each transient signal was converted into Au mass, and the mass histograms are shown in Fig. 3. In group 1, the actual volumes of the two AuNMs were consistent within a 1% margin of error. However, the measured masses deviated unexpectedly. This deviation was mainly attributed to the approximately 5-fold difference between the detected mass and the actual mass of nanorods. Hence, we calculated the detection efficiency of AuNMs by comparing the detected and actual masses of individual NMs. The detection efficiencies were lower than 100% for all AuNMs examined. The approximately 3.5-fold difference in detection efficiency between 100 nm nanospheres and nanorods was notable (Table 3).

We present two possible reasons for the reduced detection efficiency: lower ionization efficiency in the ICP and nonlinear detector response in the pulse counting mode.[26] Because we analyzed AuNMs with similar volumes, the nonlinear detector response due to the dead time of the electron multiplier should also occur for the nanospheres. In addition, the signal detection mode should automatically switch from pulse to analog when the signals exceed 10^7 cps. Therefore, we excluded the possibility of a nonlinear detector response due to dead time. The low signal intensity of nanorods compared to 100 nm nanospheres in AF4-ICP-MS (Fig. 1) supported the incomplete ionization in the ICP. In group 2, the actual volume of the two AuNMs differed by 16%. Therefore, the average mass of the 120 nm nanospheres should

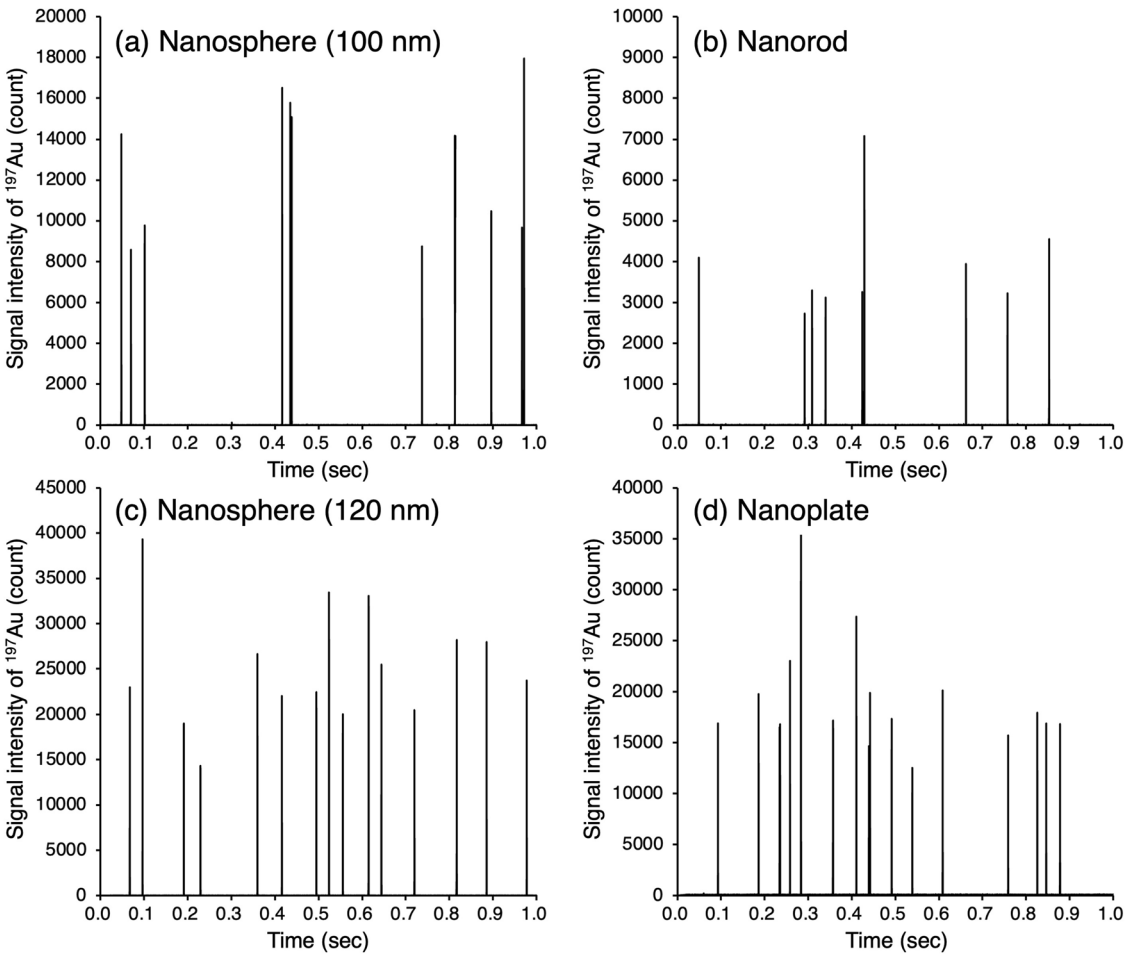

Fig. 2 Signal profiles of AuNMs in fast time-resolved analysis: nanospheres (100 nm), (a), nanorods (b), nanospheres (120 nm), (c), and nanoplates (d).

theoretically be higher than that of the nanoplates. However, the observed differences in Au mass exceeded 16%, possibly due to the lower ionization efficiency of the nanoplates than the nanospheres. Although the actual volume of 120 nm nanospheres is 16% higher than that of nanoplates, 114 nm nanospheres, which have the same volume as the nanoplates, are expected to exhibit a detection efficiency between 70.3% (100 nm) and 81.1% (120 nm). This range is still higher than the detection efficiency of 63.6% observed in the nanoplates. Incomplete ionization of particulate materials has been reported not only for microparticles[27] but also for nanoparticles.[28,29] The low ionization efficiency seen in nanorods and nanoplates can be attributed to their large specific surface areas compared to nanospheres (Table 1 and Fig. 4). Because heat dissipates from the material surface, a larger specific surface area can hinder efficient heating, thereby preventing complete vaporization and ionization of metal particles. It should be noted that ionization efficiency may decrease in large microparticles as the total energy required for ionization increases despite their low specific surface area. In addition, sufficiently small NMs should be completely ionized regardless of their shapes. Therefore, a negative correlation can be observed among shape-distinct NMs with a specific diameter range. The behavior of NMs in the ICP, such as vaporization and subsequent diffusion of atoms and/or ions, differs from that of aerosols from liquid

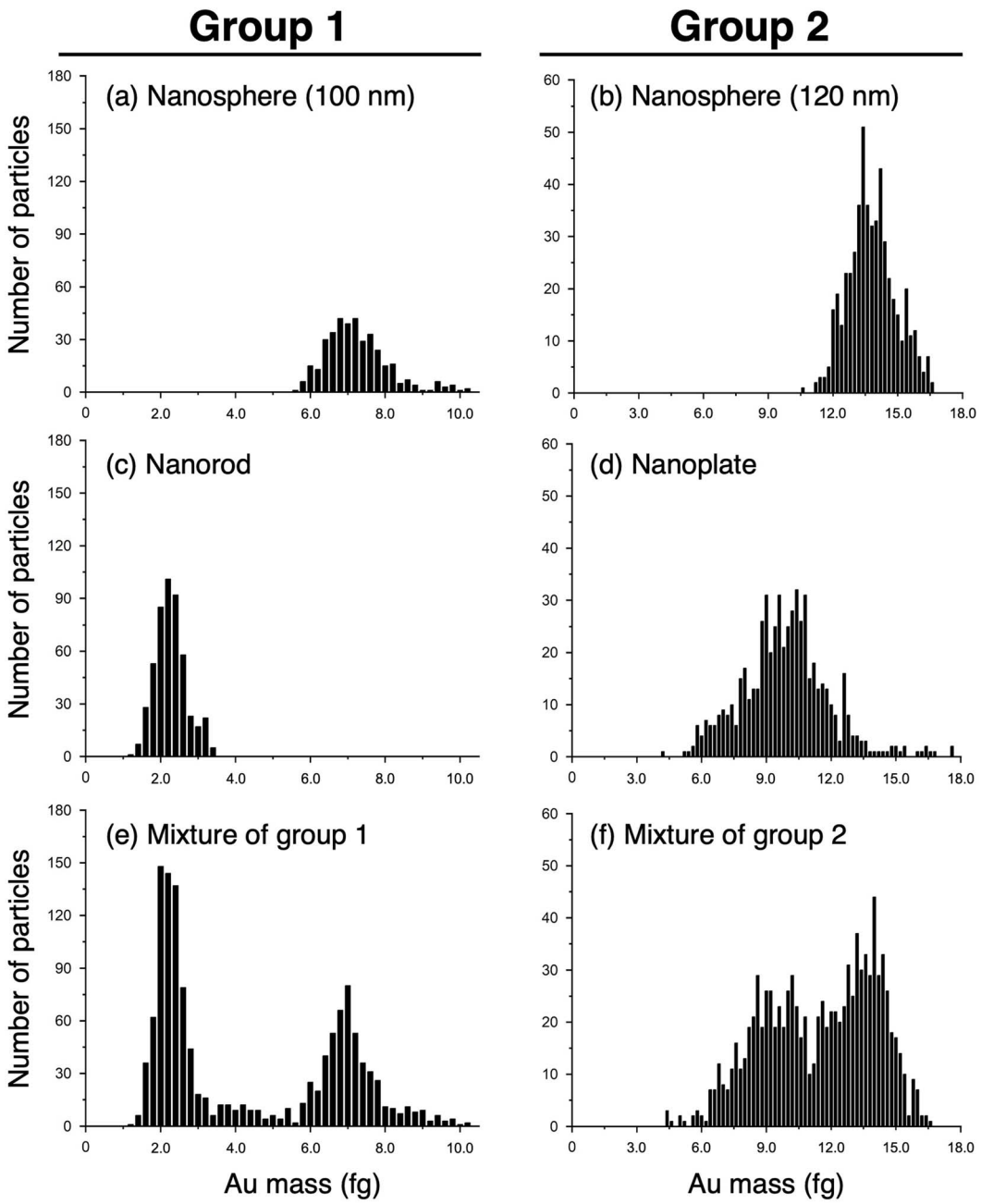

Fig. 3 Mass histograms of AuNMs in spICP-MS analysis: nanospheres (100 nm), (a), nanospheres (120 nm), (b), nanorods (c), nanoplates (d), mixture of nanospheres (100 nm) and nanorods (e), and mixture of nanospheres (120 nm) and nanoplates (f).

Table 3 Transport and detection efficiencies of AuNMs in spICP-MS

	Group 1		Group 2	
	Sphere (100 nm)	Rod	Sphere (120 nm)	Plate
Transport efficiency (%)	33.6 ± 2.1	46.2 ± 4.7	43.5 ± 8.3	54.5 ± 5.9
Average mass (fg)	7.1 ± 0.1	2.1 ± 0.1	14.2 ± 0.4	9.6 ± 0.3
Actual mass (fg)	10.1	10.0	17.5	15.1
Detection efficiency (%)	70.3	21.0	81.1	63.6

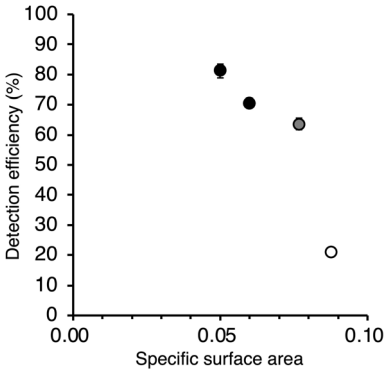

Fig. 4 Relationship between specific surface area and detection efficiency. Black circle: nanospheres, gray circle: nanoplates, white circle: nanorods.

samples, complicating accurate calibration using ionic standard solutions.[29] This discrepancy can also contribute to the large deviations of the measured masses from the actual mass. Regarding the nanospheres, the average diameters were calculated to be 59.2 ± 5.6 nm for 100 nm and 114.2 ± 9.1 nm for 120 nm particles, respectively, which are smaller than the actual particle diameters due to incomplete ionization. However, the relative standard deviations were comparable to those of the particle diameters provided by the manufacture (*i.e.*, 100 ± 8 nm and 120 ± 10 nm). Therefore, the observed variations in mass appear to reflect variations in the actual particle size rather than analytical uncertainties.

Consequently, we unexpectedly achieved the separation of differently shaped NMs with similar volumes by spICP-MS. Although shape-dependent reductions in detection efficiency hamper the precise determination of the actual mass and size of NMs, this feature is useful for distinguishing differently shaped NMs of known sizes. When an unknown sample is separated by size using AF4 and the NMs in the collected fractions are analyzed by spICP-MS, the presence of NMs with different shapes can be assessed. Consequently, combining AF4-ICP-MS data, which provide hydrodynamic size information, with spICP-MS data enables more comprehensive characterization of NMs.

Conclusions

In this study, we examined the separation of differently shaped AuNMs with similar volumes using ICP-MS-based analytical methods. Although AF4 is applicable to size-based separation of NMs, clear separation of NMs with similar volumes but different shapes was not achieved using AF4-ICP-MS because of their similar behaviors in the AF4 channel. In contrast, the signal intensities of each NM derived from spICP-MS provided a clear distinction between NMs with similar volumes. These results suggest that the combination of AF4 separation with subsequent spICP-MS analysis is a valuable approach for the detection and characterization of differently shaped NMs. Further studies are needed to clarify the applicability of this method to NMs other than gold and to NM-containing real samples.

Author contributions

Yu-ki Tanaka: conceptualization, methodology, validation, formal analysis, investigation, visualization, writing – original draft, funding acquisition. Sana Hasegawa: formal analysis, investigation, visualization, writing – review & editing. Yasumitsu Ogra: supervision, writing – review & editing, funding acquisition.

Conflicts of interest

The authors declare no conflicts of interest.

Data availability

The data supporting this article are provided in the supplementary information (SI), which includes CSV files containing the fractogram data shown in Fig. 1, time-resolved signal profiles in Fig. 2, and histograms in Fig. 3. Supplementary information is available. See DOI: https://doi.org/10.1039/d5ja00468c.

Acknowledgements

This study was supported by JSPS KAKENHI grant numbers 22K15260, 24H00749, and 25K15453.

References

1 W. J. Stark, P. R. Stoessel, W. Wohlleben and A. Hafner, *Chem. Soc. Rev.*, 2015, **44**, 5793–5805.
2 Y. Arai, T. Miyayama and S. Hirano, *Toxicology*, 2015, **328**, 84–92.
3 J. Moon, J. I. Kwak and Y.-J. An, *Chemosphere*, 2019, **215**, 50–56.
4 Y.-K. Tanaka and Y. Ogra, *Arch. Toxicol.*, 2024, **98**, 769–777.

5 Y. Xie, D. Liu, C. Cai, X. Chen, Y. Zhou, L. Wu, Y. Sun, H. Dai, X. Kong and P. Liu, *Int. J. Nanomed.*, 2016, **11**, 3557–3570.
6 X. Yang, A. P. Gondikas, S. M. Marinakos, M. Auffan, J. Liu, H. Hsu-Kim and J. N. Meyer, *Environ. Sci. Technol.*, 2012, **46**, 1119–1127.
7 Y. Suzuki, M. Kondo, M. Harimoto, Y. Okamoto, Y.-K. Tanaka, Y. Ogra and H. Akiyama, *J. Anal. At. Spectrom.*, 2024, **39**, 190–203.
8 S. Yamashita, A. Miyake and T. Hirata, *J. Anal. At. Spectrom.*, 2020, **35**, 2834–2839.
9 S. Yamashita, Y. Yoshikuni, H. Obayashi, T. Suzuki, D. Green and T. Hirata, *Anal. Chem.*, 2019, **91**, 4544–4551.
10 Y.-K. Tanaka, S. Hasegawa and Y. Ogra, *Talanta*, 2025, **293**, 128116.
11 D. Müller, S. Cattaneo, F. Meier, R. Welz and A. J. deMello, *Front. Chem.*, 2015, **3**, 45.
12 M. V. Taboada-López, D. Bartczak, S. Cuello-Núñez, H. Goenaga-Infante, P. Bermejo-Barrera and A. Moreda-Piñeiro, *Talanta*, 2021, **232**, 122504.
13 H. E. Taylor, J. R. Garbarino, D. M. Murphy and R. Beckett, *Anal. Chem.*, 1992, **64**, 2036–2041.
14 D. Ojeda, D. Bartczak, M. Singh, P. Hancock and H. Goenaga-Infante, *J. Anal. At. Spectrom.*, 2024, **39**, 1813–1823.
15 B. Bocca, E. Sabbioni, I. Mičetić, A. Alimonti and F. Petrucci, *J. Anal. At. Spectrom.*, 2017, **32**, 616–628.
16 D. Itabashi, R. Murao, S. Taniguchi, K. Mizukami, H. Takagi and M. Kimura, *ISIJ Int.*, 2020, **60**, 979–987.
17 K. G. Wahlund and J. C. Giddings, *Anal. Chem.*, 1987, **59**, 1332–1339.
18 S. López-Sanz, N. R. Fariñas, M. Zougagh, R. d. C. R. Martín-Doimeadios and Á. Ríos, *J. Anal. At. Spectrom.*, 2020, **35**, 1530–1536.
19 Y.-K. Tanaka, R. Iida, S. Takada, T. Kubota, M. Yamanaka, N. Sugiyama, Y. Abdelnour and Y. Ogra, *ChemBioChem*, 2020, **21**, 3266–3272.
20 R. Beckett and J. C. Giddings, *J. Colloid Interface Sci.*, 1997, **186**, 53–59.
21 H. El Hadri, J. Gigault, J. Tan and V. A. Hackley, *Anal. Bioanal. Chem.*, 2018, **410**, 6977–6984.
22 J. Gigault, T. J. Cho, R. I. MacCuspie and V. A. Hackley, *Anal. Bioanal. Chem.*, 2013, **405**, 1191–1202.
23 B. M. I. van der Zande, J. K. G. Dhont, M. R. Böhmer and A. P. Philipse, *Langmuir*, 2000, **16**, 459–464.
24 B. Behdani, S. Monjezi, M. J. Carey, C. G. Weldon, J. Zhang, C. Wang and J. Park, *Biomicrofluidics*, 2018, **12**, 051503.
25 J. Park and A. Mittal, *Chromatography*, 2015, **2**, 472–487.
26 I. Strenge and C. Engelhard, *J. Anal. At. Spectrom.*, 2020, **35**, 84–99.
27 P. Goodall, M. E. Foulkes and L. Ebdon, *Spectrochim. Acta, Part B*, 1993, **48**, 1563–1577.
28 W.-W. Lee and W.-T. Chan, *J. Anal. At. Spectrom.*, 2015, **30**, 1245–1254.
29 K.-S. Ho, K.-O. Lui, K.-H. Lee and W.-T. Chan, *Spectrochim. Acta, Part B*, 2013, **89**, 30–39.

